

Statistical harmonization and uncertainty assessment in the comparison of satellite and radiosonde climate variables

F. Finazzi¹  | A. Fassò¹ | F. Madonna² | I. Negri¹ | B. Sun³ | M. Rosoldi²

¹Department of Management,
Information and Production Engineering,
University of Bergamo, Bergamo, Italy

²Institute of Methodologies for
Environmental Analysis, National
Research Council of Italy, Rome, Italy

³IMSG, NOAA Center for Satellite
Applications and Research,
Washington, DC

Correspondence

F. Finazzi, Department of Management,
Information and Production Engineering,
University of Bergamo, 24044 Bergamo,
Italy.
Email: francesco.finazzi@unibg.it

Funding information

GAIA-CLIM project, Grant/Award
Number: 640276

Abstract

Satellite product validation is a key to ensure the delivery of quality products for climate and weather applications. To do this, a fundamental step is the comparison with other instruments, such as radiosonde. This is especially true for essential climate variables such as temperature and humidity.

Thanks to a functional data representation, this paper uses a likelihood-based approach that exploits the measurement uncertainties in a natural way. In particular, the comparison of temperature and humidity radiosonde measurements collected within the network of the Universal Rawinsonde Observation Program (RAOB) and the corresponding atmospheric profiles derived from the infrared atmospheric sounding interferometer aboard MetOp-A and MetOp-B satellites is developed with the aim of understanding the vertical smoothing mismatch uncertainty.

Moreover, conventional RAOB functional data representation is assessed by means of a comparison with radiosonde reference measurements given by the Global Climate Observing System (GCOS) Reference Upper-Air Network (GRUAN), which provides high-resolution fully traceable radio-sounding profiles. In this way, the uncertainty related to coarse vertical resolution, or sparseness, of the conventional RAOB is assessed.

It has been found that the uncertainty of vertical smoothing mismatch averaged along the profile is 0.50 K for temperature and 0.16 g/kg for water-vapor mixing ratio. Moreover, the uncertainty related to RAOB sparseness, averaged along the profile, is 0.29 K for temperature and 0.13 g/kg for water-vapor mixing ratio.

KEYWORDS

climate change, maximum likelihood, satellite kernel, spatio-temporal mismatch, splines, vertical profiles

1 | INTRODUCTION

Satellite validation is a key to ensure that satellite products meet the mission-specified requirements for climate and weather applications. Because the agreement of satellite measurements with ground-based reference measurements is an essential quality indicator, one major issue in performing a rigorous validation is the quantification of the uncertainty due to the co-location mismatch in time and space between satellite- and ground-based reference observations. This mismatch is due to the different sampling of atmosphere carried out by the two instruments (Verhoelst et al., 2015), which are also quite often based on very different sensing techniques and may be affected by bias and/or calibration

error. Moreover, satellite- and ground-based observations are typically collected on very different time scales and spatial scales. As a consequence, in a satellite versus ground measurements comparison, we may have horizontal, vertical, and/or temporal mismatches in smoothing and/or profile resolution. These mismatches, together with comparator uncertainty, contribute to the overall co-location mismatch uncertainty (hereinafter mismatch uncertainty).

Over the last decade, several authors have tried to estimate the impact of the satellite- versus ground-based mismatch uncertainty of the essential climate variables (ECVs). The most common approach is to use simple descriptive statistics to identify the maximum temporal and spatial distances, which warrant a controlled mismatch uncertainty; see, for example, the work of Pappalardo et al. (2010) for aerosols and the work of Kursinski and Hajj (2001) for water vapor. Moreover, considering vertical resolution, Pougatchev et al. (2009) found that, when available, the averaging kernels can be used to reconcile the vertical resolution of satellite- and ground-based observations of temperature and humidity.

A rigorous metrological characterization of the mismatch uncertainty requires the quantification of the total uncertainty budget for each satellite-retrieved ECV. Hence, the uncertainty budget includes the contribution of random systematic sampling and smoothing uncertainties, and their correlation with all the relevant environmental factors. Pioneering works in this direction are of Ridolfi et al. (2007) and Lambert and Vandenbussche (2011). More recently, Verhoelst et al. (2015) have used an explicit physic simulation method for computing a full uncertainty budget closure for ozone. Moreover, Fassò, Ignaccolo, Madonna, Demoz, and Franco-Villoria (2014) and Ignaccolo, Franco-Villoria, and Fassò (2015) proposed an approach based on the extension of the classical functional regression model able to cover for heteroskedasticity of mismatch error in temperature and humidity observation.

The GAIA-CLIM project (www.gaia-clim.eu) is a Horizon 2020 project that aims at improving the use of nonsatellite measurements to characterize, calibrate and validate satellite measurements. Considering temperature and humidity, one of its objectives is to understand the mismatch uncertainty in the comparison of the satellite observations obtained by the infrared atmospheric sounding interferometer (IASI) instrument, on board EUMETSAT MetOp-A and MetOp-B, with the radiosonde observations (RAOBs). In fact, RAOB profiles are appealing for satellite validation because of their extensive spatial and temporal coverage, hence permitting the assessment of mismatch uncertainty at a global level. Despite this, RAOB observations cannot be strictly considered reference measurements because they are not fully traceable and have a limited vertical resolution; see the work of Dirksen et al. (2014). Note that the Global Climate Observing System Reference Upper-Air Network (GRUAN, www.gruan.org) provides reference products, which are fully traceable but have a very limited spatial coverage (16 sites as the paper is written).

Along these lines, this paper focuses on the vertical smoothing mismatch uncertainty of IASI–RAOB profile comparison of temperature and humidity. This objective is achieved by a statistical technique for vertical harmonization, which is independent of the availability of IASI averaging kernels, hence especially relevant for comparisons where averaging kernels are not available, in particular for historical data analysis. To do this, the vertical data-point sparseness of a RAOB network is assessed by means of a comparisons with GRUAN reference products where available.

The proposed technique is a two-step technique. At the first step, RAOB profiles are transformed into continuous functions using splines, which are optimized to match as close as possible to GRUAN profiles. In doing this, vertical sparseness uncertainty and processing mismatch uncertainty are assessed. At the second step, RAOB profiles are harmonized by considering weighting functions based on the generalized extreme value (GEV) probability density function (pdf) whose parameters depend on the IASI levels.

The paper is structured as follows. In Section 2, data from both satellite (IASI) and radiosonde (GRUAN and RAOB) are introduced. In Section 3, the various sources of uncertainty arising in satellite-ground comparisons are reviewed. Sections 4 and 5 discuss novel statistical modeling: The former section leverages on intuition, whereas the latter embeds the same model in a rigorous maximum likelihood estimation approach. Section 6 applies this approach to IASI–RAOB comparison for a number of RAOB stations in Central Europe. To do this, in Section 6, the RAOB soundings are transformed into functional data and harmonized to match IASI vertical smoothing. Then, the sparseness uncertainty of RAOB and vertical smoothing uncertainty of IASI–RAOB comparison are computed. Section 7 gives concluding remarks.

2 | DATA SETS

The data sets used in this study include atmospheric profile retrievals derived from an IASI instrument and from conventional (RAOB) and reference (GRUAN) radiosonde networks. The RAOB–IASI co-location data set, which is provided by NOAA-NESDIS, has been collected through the NOAA Products Validation System (NPROVS); see Sun et al. (2017) (<http://www.star.nesdis.noaa.gov/smcd/opdb/nprovs/>). The NPROVS data set used in this study includes $K = 3,908$

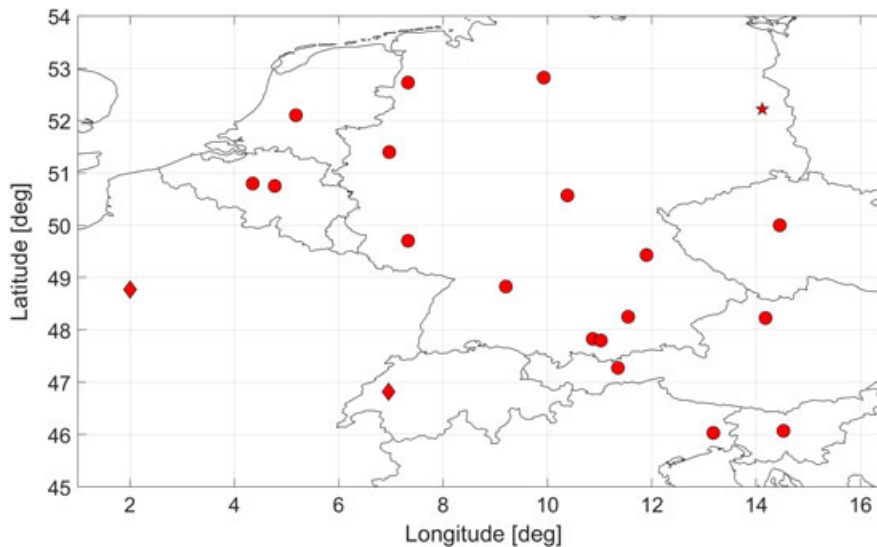


FIGURE 1 Spatial distribution of RAOB stations in Central Europe. Circles are VAISALA RS92 launching stations, and diamonds are non-VAISALA stations. The star denotes the GRUAN-RAOB station in Lindenberg. GRUAN = Global Climate Observing System Reference Upper-Air Network; RAOB = radiosonde observation

co-located profiles at 21 RAOB stations selected across the Central European area (C-EU), described in Figure 1, for the period January 2015 to February 2016.

Each co-location pair includes RAOB and IASI profiles for temperature and water-vapor mixing ratio (WVMR) with RAOB at mandatory and significant levels and IASI at 100 levels. In order to consider profiles with enough data, the data set has been filtered as follows: Temperature (WVMR) has been restricted to atmospheric range 958.6 – 10 hPa (958.6 – 300 hPa), and only co-locations with at least 20 (14) RAOB measurements have been selected for the analysis, giving $K = 1,596$ (2648) co-locations out of the original $K = 3,908$ NPROVS co-locations. Notice that the atmospheric range considered after filtering is still relevant for climate and weather studies as pressure levels 10 hPa and 300 hPa, corresponding to around 40 km and 10 km, respectively.

In addition, the GRUAN station at Lindenberg has been used as a reference for radio-sounding measurements to understand conventional RAOB sparseness uncertainty. In fact, this GRUAN station is also a conventional RAOB station and, although the instrument is physically the same for both, data are processed in a different manner, giving different measurements. Because the difference between GRUAN and RAOB measurements depends only on the processing, we claim that the RAOB sparseness uncertainty is representative of the whole geographic area considered in this paper, provided that measurements are taken using Vaisala RS92 instruments. As a result, for temperature (WVMR) we have $K_G = 306$ (396) GRUAN-RAOB co-locations.

Other meteorological variables considered in statistical modeling of the mismatch error, such as wind, solar radiation or geopotential, have been taken from the ERA-Interim global atmospheric reanalysis implemented by the European Centre for Medium-Range Weather Forecasts (ECMWF); see the work of Berrisford et al. (2009).

2.1 | IASI

Products retrieved from EUMETSAT's IASI instruments aboard of MetOp-A and MetOp-B satellites considered in this study are based on version 6 of the EUMETSAT IASI level-2 processor. The IASI is a Fourier transform spectrometer based on the Michelson interferometer, associated with an integrated imaging system (Blumstein et al., 2004).

The IASI atmospheric profiles of temperature (WVMR) are available at 74 (32) pressure levels in the range 958.6–10 hPa (958.6 – 300 hPa). Considering vertical smoothing, the IASI sounding products represent thermodynamic states of deep atmospheric layers at variable depths, due to the integrating nature of the radiation measurements at the top of the atmosphere. The maximum number of independent pieces of information is approximately 14 (10) for temperature (humidity) profiles, the exact number depending on atmospheric conditions. Hence, the true vertical resolution is considerably lower than the vertical grid of 74 (32) pressure levels discussed above, and profiles retrieved from such radiance measurements are smoothed versions, where the smoothing functions are given by the so-called averaging kernels. Although version 6 of

the IASI level-2 processor provides the information to calculate the averaging kernels, it has not been used in this paper, being unavailable in the NPROVS data set.

2.2 | Conventional RAOB

Conventional RAOBs have been used historically as a de facto standard data set in satellite calibration (via radiative transfer models) and validation. Worldwide, there are more than 2,000 radiosonde launch sites and mobile ship-based launch stations.

While a radiosonde transmits an essentially continuous stream of temperature and humidity information back to the station (each 5–10 m of altitude, measured each 1–2 s), for temperature (WVMR), a RAOB data set includes only 15 (6) “mandatory levels” in the atmospheric range 958.6 – 10 hPa (958.6 – 300 hPa). Moreover, data are given at various “significant levels,” which are the pressure levels where a significant change or an extreme is identified in the vertical temperature and/or dewpoint temperature profiles. For this reason, the ECV variation between two such significant levels is often assumed close to linear. In practice, altitude and number of significant levels change among different profiles and, on average, 28 significant levels per profile are available in the RAOBs collected at NPROVS, the exact numbers depending on specific atmospheric conditions.

Considering sensor type, it is worth mentioning that, for the area considered, the RAOB stations are mainly based on Vaisala RS92 sondes, with two remarkable exceptions: SRS sondes in Switzerland and MODEM sondes in France (see Figure 1).

2.3 | GRUAN

Conventional RAOBs may not be able to provide reference-quality in situ and ground-based remote sensing observations of upper-air ECVs for metrological and traceability reasons; see the works of Seidel, Sun, Petey, and Reale (2011), Immeler et al. (2010), and Bojinski et al. (2014). Improving on this, GRUAN data processing was developed to meet the criteria for reference measurements (Dirksen et al., 2014). As a result, GRUAN radio-sounding profiles are provided together with individual measurement uncertainty estimates at high vertical/temporal resolution: Measurements are obtained at 1–2 s or 5–10 m in altitude; this temporal resolution is then reduced to about 10 s during processing by a low-pass filter to avoid temperature spikes. GRUAN quality has been extensively assessed (see, e.g., Calbet et al., 2017). Because the Lindenberg GRUAN station is also a conventional RAOB station, it is important to remark here that, considering this station, the two profiles differ for the vertical resolution and for data processing. In fact, the former is obtained using the GRUAN processing algorithm whereas the latter is obtained using the algorithm implemented in Vaisala RS92 instruments. As a result, the two products give noncoinciding measurements.

3 | CO-LOCATION MISMATCH SOURCES

As discussed above, the comparison of radiosonde and IASI profiles aims at understanding which factors contribute to the discrepancies observed between a satellite vertical profile and a comparator profile. Although ideally, the comparator should be an error-free “true” state, in practice, its uncertainty is worth to be considered.

In fact, a meaningful comparison should take into account the spatio-temporal mismatch between profiles; the different vertical smoothing and resolution of the two instruments/data sets; the different horizontal smoothing and resolution of the two instruments; and the comparator uncertainty, in particular radiosonde instruments issues, including solar radiation, dry-bias when measuring humidity, ventilation effects, ground calibration effects, and all the other problems detailed in the work of Dirksen et al. (2014).

The following subsections briefly discuss the former points justifying a focus on vertical smoothing uncertainty based on data harmonization.

3.1 | Satellite smoothing

As discussed in Section 2, radiosonde and IASI are based on completely different measurement techniques. While the radiosonde is able to make a “direct” measurement of the ECV at the position in space and time reached by the weather

balloon, IASI sounds the atmosphere using an interferometry technique. This implies that the vertical resolution of IASI is much lower than the resolution characterizing a radiosonde. Any comparison between radiosonde and IASI profiles, thus, may be affected by these differences.

Note that different methods are available in satellite product validation to resolve the issue in vertical resolution difference. One requires to apply satellite sounder averaging kernels to the target data, for example, radiosonde data, and then to compare with the retrievals (Maddy & Barnet, 2008); one is to first average a vertical layer for both satellite and target data profiles and, then, to compute the validation statistics at those “coarse” vertical layers (Sun et al., 2017; Tobin et al., 2006). In this study, we choose to employ the vertical harmonization technique for the uncertainty assessment (see Section 4).

Considering horizontal smoothing, note that IASI samples a limited atmospheric cone, with a footprint of about 12 km. Hence, the co-location mismatch due to the variability of the atmosphere within the portion of the atmosphere sampled may be assumed small when considering the total co-location uncertainty and negligible considering the effect on vertical smoothing uncertainty following the considerations of Section 3.4 below.

3.2 | Spatio-temporal mismatch

Radiosonde and IASI profiles are characterized by a spatio-temporal mismatch. For the data set considered, only co-locations with horizontal distances up to 300 km at surface and time delays up to three hours have been considered; see the work of Kursinski and Hajj (2001). This is because weather balloon launches are not perfectly synchronized with the satellite overpasses, and overpasses may be far from the station where the radiosonde is launched, both in space and time. Additionally, the IASI profile is retrieved nearly instantly. On the other side, according to Seidel et al. (2011), weather balloons take on average 1.7 hr from the surface up to 10 hPa and typically shift up to 50 km in the lower stratosphere, although there is considerable variability due to variability in climatological winds.

Although relevant, the effect of the spatio-temporal mismatch is not explicitly studied in this paper. In fact, this was done in the work of Fassò, Verhoelst, and Lambert (2018) where, applying a isotonic bivariate regression model to the harmonized RAOB data, the increase in uncertainty with respect to horizontal distance and time mismatch is assessed using a harmonization approach similar to this paper. For the current paper, one can see that ignoring this effect inflates the total uncertainty estimates. On the other side, the effect on a vertical smoothing uncertainty estimate is limited and discussed below in Section 3.4 and in the case study.

3.3 | Comparator uncertainty and vertical sparseness

It has been seen that RAOB data are at subreference level and are provided at the so-called mandatory and significant pressure levels, which are sparse vertically. The latter being given at pressure levels where some interesting variation is happening. This entails that data occur according to a preferential sampling design (Diggle, Menezes, & Su, 2010), which is dependent on second-order derivatives.

As a consequence, before developing an IASI comparison, the estimation of the “true” profile at any pressure level, based on RAOB data, requires a statistical assessment. In this frame, (vertical) sparseness uncertainty is the uncertainty component related to the coarse vertical resolution.

In addition, the comparator uncertainty is inflated by instrument issues. These include solar radiation, dry bias when measuring humidity, instrument time lag, ventilation effects, processing algorithm version, and ground calibration effects. We do not enter in technical details here, but refer to the work of Dirksen et al. (2014). Instead, we mention here that a total sensor/processing bias will be considered in this paper. Nonetheless, because this bias will be estimated using a GRUAN–RAOB comparison at Lindeberg station, it will depend on sonde type and will be not generalizable to all RAOB networks. For this reason, the total uncertainty of the comparisons will include this component.

3.4 | Discussion

Ideally, a full metrological budget would include and quantify all above uncertainty components. Although this objective overwhelms this paper for reasons of data availability and paper length, some of the related issues are considered in other papers as discussed above. Along these lines, it is clear that the above mismatch sources may inflate the total uncertainty

of the IASI–RAOB comparison. Despite of this, we will see that the effect of the above sources on vertical smoothing uncertainty is minor, and it is neglectable under error incorrelation assumptions.

4 | STATISTICAL HARMONIZATION AND UNCERTAINTIES

Vertical harmonization refers to a data transformation, which reduces the differences in the vertical smoothing between the two profiles and improves the radiosonde and IASI profiles' comparability. In our case, the low vertical resolution of IASI implies that IASI retrievals are much smoother than radiosonde data. Because we cannot unsmoothen IASI profiles, the radiosonde profiles are smoothened in order to mimic the IASI retrievals.

This is achieved by the convolution of the radiosonde profile $s(p)$ of temperature and humidity with a normalized weighting function $w(p; p')$ in the observed pressure P_R range defined in Section 2. Namely,

$$\tilde{s}(p) = \int_{P_R} s(q)w(q; p)dq \quad (1)$$

with $\int_{P_R} w(q; p)dq = 1$.

The “true” profile may be assumed a continuous function of pressure, but RAOB profiles are observed only at a limited number of “preferential” levels. To handle this, a two-step procedure is proposed. The first step, developed in Section 4.2, extends the idea of Fassò et al. (2014) to represent atmospheric profiles as functional data (Ramsay & Silverman, 2012) with a smoothness coefficient obtained by minimizing the difference with the reference GRUAN data. The second step, described in Sections 4.3 and 4.4, optimizes the weighting function w .

4.1 | Data and likelihood function

Let us consider a collection of K co-located RAOB–IASI profiles observed across the geographic area and time frame of interest, with a subset of these K co-locations, for example, $\{1, \dots, K_G\}$, obtained at the Lindenberg station, and having GRUAN profile counterparts.

For each given co-location $k = 1, \dots, K$, let $\mathbf{x}_{J,k}$ be the radiosonde data vector related to pressure levels $\mathbf{p}_{J,k} = (p_{J,k,1}, \dots, p_{J,k,N_{J,k}})$, with $J = R$ for RAOB or $J = G$ for GRUAN, and $N_{J,k}$ be the number of pressure levels for co-location k . Moreover, let $\mathbf{x}_{I,k}$ be the IASI data vector related to pressure levels $\mathbf{p}_I = (p_{I,1}, \dots, p_{I,M})$, with M as the number of IASI pressure levels. Note that the RAOB pressure levels depend on co-location k . Instead, IASI pressure levels are invariant among co-locations with $M = 74$ (32) for temperature (WVMR). As a consequence, RAOB and IASI pressure levels are different and vertical matching may represent an issue. On the contrary, the number of GRUAN measurements $N_{G,k}$ is very high for all profiles so that, for any prefixed RAOB level in $\mathbf{p}_{R,k}$, a very close GRUAN pressure level in $\mathbf{p}_{G,k}$ may be found.

4.2 | RAOB estimation and sparseness uncertainty

The discrepancies between conventional RAOB and GRUAN may be used to understand the loss of information of RAOB due to its sparse vertical resolution. In fact, the minimization of this loss can be used to define an optimal estimate of the unobserved true signal.

To see this, the true signal of the k th profile is considered as a smooth function denoted by $s_k^0(p)$, and it is related to observation $x_{J,k}(p)$ for $p \in \mathbf{p}_J$ and $J = R, G, I$ by the following conditions:

$$x_{J,k}(p) = s_{J,k}(p) + \varepsilon_{J,k}(p), \quad (2)$$

where $\varepsilon_{J,k}(p)$ is Gaussian distributed, $N(0, \sigma_{J,k}^2(p))$, and

$$s_{G,k}(p) = s_k^0(p)$$

$$s_{R,k}(p) = s_k^0(p) + \Delta(p) \quad (3)$$

$$s_I(p) = \int_{P_R} s_k^0(q)w(q; p)dq. \quad (4)$$

These three conditions will be discussed in detail later. For the moment, note that $\Delta(p)$ is a smooth bias, constant over co-locations, and w is a weighting function. Moreover, note that, for GRUAN, the squared measurement uncertainty $u_G^2(p) = E(x_G(p) - s^0(p))^2$ is known at all pressure levels $p \in \mathbf{p}_G$ and $u_G^2 = \sigma_G^2$. For RAOB, the measurement uncertainty $u_R^2 = \sigma_R^2 + \Delta^2$ is not widely available, but there is some evidence that $\sigma_{R,j}^2(p) \cong \rho \sigma_{G,j}^2(p)$ for some $\rho \geq 1$. For simplicity, we assume that ρ does not depend on pressure level p or on co-location k .

In this paper, we estimate the smooth profile $s_R(p)$ by $\hat{s}_R(p, \lambda)$, which is a penalized spline with smoothing factor λ . The estimated profile $\hat{s}_R(p; \lambda)$ is computed on RAOB data by solving the following penalized weighted least square problem:

$$\hat{s}_{R,k}(p; \lambda) = \arg \min_s \left[\sum_{j=1}^{N_{R,k}} (x_{R,k}(p_j) - s(p_j))^2 \alpha_{R,k}(p) + \lambda \sum_{j=1}^{N_{R,k}} \left(\frac{\partial^2 s(p_j)}{\partial p^2} \right)^2 \alpha_{R,k}(p) \right], \quad (5)$$

where

$$\alpha_{R,k}(p) = \alpha_{G,k}(p) = u_{G,k}(p)^{-2} / \sum_{k=1}^{K_G} u_{G,k}(p)^{-2} \quad (6)$$

for co-locations in Lindeberg and $\alpha_R = \frac{1}{N_{R,k}}$ elsewhere.

Following, for example, the work of Reinsch (1971), and using one knot per observation, the solution $\hat{s}_{R,k}$ of equation (5) may be expressed in terms of tolerance $\tau = \tau(\lambda)$, which is the upper limit of the weighted root mean square error along the RAOB profile

$$\frac{1}{N_{R,k}} \sum_{p \in \mathbf{p}_{R,k}} |x_{R,k}(p) - \hat{s}_R(p, \lambda)|^2 \alpha_{R,k}(p) \leq \tau^2, \quad (7)$$

where, clearly, $\tau = 0$ gives interpolating splines. For this reason, depending on the context, we will use either τ or λ to address smoothing properties of spline $\hat{s}_{R,k}(p, \lambda) = \hat{s}_{R,k}(p, \tau)$.

Using GRUAN–RAOB comparison at Lindenbergl, we estimate the bias Δ by the weighted GRUAN–RAOB average difference, namely,

$$\hat{\Delta}(p, \tau) = \sum_{k=1}^{K_G} (\hat{s}_R(p; \tau) - x_{G,k}(p)) \alpha_{G,k}(p). \quad (8)$$

Next, the smoothing factor $\lambda(\tau)$ is obtained by optimizing the adjusted GRUAN–RAOB difference. In other words, τ is the solution of the following weighted least squares criterion:

$$\hat{\tau} = \arg \min_{\tau} \sum_{k=1}^{K_G} \sum_{p \in \mathbf{p}_{G,k}} [x_{G,k}(p) - (\hat{s}_R(p; \tau) - \hat{\Delta}(p; \tau))]^2 \alpha_{G,k}(p), \quad (9)$$

where α_G is defined in Equation (6).

Due to the peculiarity of the RAOB sampling points discussed in Section 2.2, three spline models are compared in Section 6: linear and cubic smoothing Bsplines and Hermite interpolating splines (Hsplines). The former two are well known, and we only remark here that the smoothing coefficient τ is not obtained by a cross-validation or generalized cross-validation criterion on RAOB data as in standard smoothing splines. Instead, τ is numerically optimized according to the GRUAN agreement criterion (9), which takes into account measurement uncertainty. Interpolating Hsplines are also known as piecewise cubic Hermite interpolating polynomials, being cubic monotonic splines with continuous first derivatives; see the work of Fritsch and Carlson (1980). Hence, Hsplines are introduced here as an intermediate solution between cubic and linear Bsplines. In fact, in this model selection problem, one could use also smoothing Hsplines; this approach being further discussed in the case study.

After obtaining $\hat{\tau}$, the optimized quantity in Equation (9) provides the total mismatch uncertainty profile of GRUAN–RAOB comparison, namely,

$$u_{\text{RG.tot}}^2(p) = \sum_{k=1}^{K_G} [x_{G,k}(p) - \hat{s}_R(p; \hat{\tau})]^2 \alpha_{G,k}(p), \quad (10)$$

which is the loss of information due to sparseness and difference in data processing. More comments and the decomposition of Equation (10) in sparseness and processing uncertainty will be developed in the case study.

4.3 | Vertical smoothing

With the aim of making radiosonde and IASI profiles comparable, the radiosonde profile of the previous section denoted in the sequel by $\hat{s}_R(p) = \hat{s}_R(p; \hat{\tau})$ is smoothed by means of a weighted integral, namely,

$$\tilde{s}_R(p; \theta) = \int_{p_R} \hat{s}_R(q) w(q; \theta, p) dq. \quad (11)$$

In Equation (11), the weight function $w(q; \theta, p)$ is a nonnegative and normalized weight function, depending on p and a parameter vector $\theta = \theta(p)$, which has to be estimated. Because the role of w is to mimic the IASI sounding of the atmosphere, Fassò et al. (2018) considered the following alternative functions: rectangular, sine, Gaussian, and GEV distribution. As expected, the latter was found to outperform the other simpler competitors and, for this reason, it is used here. In particular, the GEV pdf has parameter vector (μ, σ, ξ) , which are the location, scale and shape parameters, respectively; see the work of Kotz and Nadarajah (2000). In this paper, we use level-dependent parameters, namely, $\mu(p) = p$ and $\theta(p) = (\sigma(p), \xi(p))$.

In order to compute the harmonized RAOB \tilde{s} from Equation (11), we need to estimate θ and a natural choice is the following penalized weighted least squares iterated for $j = 1, \dots, M$:

$$\hat{\theta}_j = \hat{\theta}(p_j) = \arg \min_{\theta} \left[\sum_{k=1}^K [x_{I,k}(p_j) - \tilde{s}_{R,k}(p_j; \theta)]^2 \alpha_{I,k}^2(p_j) + I(j > 1) \|\theta - \hat{\theta}_{j-1}\|_{\Sigma_{\zeta}} \right], \quad (12)$$

where $p_j \in \mathbf{p}_I$ and the weight α_I^2 is the normalized squared reciprocal measurement uncertainty of IASI, analogous to formula (6). Moreover, $\|x\|_{\Sigma} = x' \Sigma^{-1} x$, where Σ_{ζ} is a variance covariance matrix to be discussed in the next section and $I(j > 1) = 1$ if $j > 1$ and $= 0$ else. Note that the penalty term in (12) is related to smoothness of the atmosphere and, hence, of $\theta(p)$ with respect to p .

4.4 | Vertical smoothing uncertainty

A byproduct of the data harmonization procedure above described is the uncertainty component related to the vertical smoothing. In particular, the RAOB-IASI mismatch uncertainty due to difference in vertical smoothing is given by

$$u_{\text{RI.vsmooth}}^2(p) = u_{\text{RI.raw}}^2(p) - u_{\text{RI.harm}}^2(p), \quad (13)$$

where $u_{\text{RI.harm}}(p)$ is the vertically harmonized mismatch uncertainty, that is,

$$u_{\text{RI.harm}}^2(p) = \sum_{k=1}^K [\tilde{s}_k(p; \hat{\theta}(p)) - x_{I,k}(p)]^2 \alpha_{I,k}(p), \quad (14)$$

and $u_{\text{RI.raw}}(p)$ is the raw mismatch uncertainty in the comparison of IASI with nonharmonized RAOB $s_R(p)$, namely,

$$u_{\text{RI.raw}}^2(p) = \frac{1}{K} \sum_{k=1}^K [x_{I,k}(p) - \hat{s}_{R,k}(p)]^2 \alpha_{I,k}(p).$$

Hence, $u_{\text{RI.vsmooth}}^2(p_j)$ may be interpreted as the (squared) mismatch uncertainty improved by the data harmonization.

Notice that, in Equation (11), one could use the adjusted RAOB $\hat{s}_R - \hat{\Delta}$, instead of \hat{s}_R . We prefer to use \hat{s}_R , because, as mentioned in Section 2.2, the RAOB network is heterogeneous, and the bias $\hat{\Delta}$ is valid only for Vaisala RS92 sondes. It follows that the uncertainties of this section are valid for the entire RAOB network considered and include the uncertainty related to sensor heterogeneity. More generally, considering the various mismatch sources of Section 3, the total uncertainty $u_{\text{RI.raw}}^2(p)$ is inflated by the smooth components of these mismatches not filtered by the spline transform $\hat{s}_{R,k}$. Moreover, note that the vertical smoothing uncertainty in Equation (13), being defined by a difference of two uncertainties, is approximately independent from all the additive uncertainty components, that is, it is not affected by the other co-location mismatch sources assuming uncorrelated errors.

5 | LIKELIHOOD INFERENCE

The modeling machinery of the previous section has a rigorous interpretation as a maximum likelihood estimation problem for a nonlinear mixed-effect model. This is properly described using three main steps for RAOB, GRUAN and IASI, respectively.

5.1 | RAOB likelihood

The first step is to represent the RAOB true signal by the following linear representation:

$$s_R(p) = \mathbf{B}(p)' \boldsymbol{\gamma}_R, \quad (15)$$

where \mathbf{B} is the vector of Bspline basis functions and $\boldsymbol{\gamma}_R$ is the vector of the spline coefficients. Using this, Equation (2) for the k th RAOB profile may be rewritten as follows:

$$x_{R,k}(p) = \mathbf{B}(p)' \boldsymbol{\gamma}_{R,k} + \varepsilon_{R,k}(p),$$

where $p \in \mathbf{p}_{R,k}$, $k = 1, \dots, K$.

Stacking $x_{R,k}(p_1), \dots, x_{R,k}(p_{N_{R,k}})$ in a vector, for example, $X_{R,k}$, all \mathbf{B}' 's in a matrix $Z_{R,k}$ and all errors in a vector ε , we have the following matrix representation:

$$X_{R,k} = Z_{R,k} \boldsymbol{\gamma}_{R,k} + \varepsilon_{R,k}.$$

This has a well-known mixed-effects model interpretation (see, e.g., Fahrmeir, Kneib, Lang, & Marx, 2013). To see this, let $[\boldsymbol{\gamma}]$ denote the probability distribution of the random vector $\boldsymbol{\gamma}$ and assume that $[\boldsymbol{\gamma}_{R,k}] = N(0, G_k)$, where $G_k = \lambda^{-2} I_k$; $\lambda > 0$ is a known smoothing factor; and I_k is the identity k -dim matrix. Then, the penalized least square criterion in Equation (5) corresponds to the maximum likelihood estimate (MLE). In fact, apart for an additive constant, we have

$$-2 \log[\boldsymbol{\gamma}_k | X_{R,k} | \boldsymbol{\gamma}_k] = \|\boldsymbol{\gamma}_k\|_{G_k} + \|X_{R,k} - Z_{R,k} \boldsymbol{\gamma}_k\|_{\Sigma_R}.$$

Stacking all $X_{R,k}$ in a vector X_R , and similarly for Z , $\boldsymbol{\gamma}$, and ε , we have the following matrix representation:

$$X_R = Z_R \boldsymbol{\gamma} + \varepsilon_R$$

and

$$\begin{aligned} -2 \log[\boldsymbol{\gamma} | X_R | \boldsymbol{\gamma}] &= \|\boldsymbol{\gamma}\|_G + \|X_R - Z_R \boldsymbol{\gamma}\|_{\Sigma_R} \\ &= \sum_{k=1}^K (\|\boldsymbol{\gamma}_k\|_{G_k} + \|X_{R,k} - Z_{R,k} \boldsymbol{\gamma}_k\|_{\Sigma_R}), \end{aligned}$$

where Σ_R is diagonal matrix corresponding to uncertainties in Equation (6). Because this likelihood is optimized by minimizing each summand independently, the computation burden is linear in K and the solution is the MLE $\hat{\boldsymbol{\gamma}}(\tau)$ as a function of τ (or λ).

Hence, Equation (5) may be rewritten as

$$\hat{s}_{R,k}(p; \tau) = \mathbf{B}(p)' \hat{\boldsymbol{\gamma}}_R(\tau).$$

Notice that the RAOB data model for X_R may be partitioned as

$$X_R = \begin{pmatrix} X_{R_1} \\ X_{R_2} \end{pmatrix} = (Z_{R_1}, Z_{R_2}) \begin{pmatrix} \boldsymbol{\gamma}_{R_1} \\ \boldsymbol{\gamma}_{R_2} \end{pmatrix} + \begin{pmatrix} \varepsilon_{R_1} \\ \varepsilon_{R_2} \end{pmatrix},$$

where R_1 is the GRUAN matching data set corresponding to co-locations $k = 1, \dots, K_G$, and R_2 is the remaining major part of the RAOB data set with $K - K_G$ soundings.

5.2 | GRUAN–RAOB likelihood

Now, considering GRUAN and RAOB matching data in R_1 , we have the following representation:

$$\begin{aligned} x_G(p) &= s_G(p) + \varepsilon_G(p) \\ s_G(p) &= s_R(p) + \Delta(p), \end{aligned}$$

where Δ is a GRUAN–RAOB fixed effect bias. Hence, in matrix notation, we may write

$$X_G = Z_{R_1} \gamma + \Delta + \varepsilon_G$$

and

$$-2 \log [X_G | X_{R_1}, \gamma_{R_1}] = \|X_G - Z_G \gamma_{R_1} - \Delta\|_{\Sigma_G}.$$

If we compute this at $\hat{\gamma}(\tau)$, we have a profile log-likelihood $l(\tau, \Delta | \hat{\gamma}(\tau))$, which is easily optimized for $\Delta(\tau)$ and, finally, for $(\tau | \hat{\Delta}(\tau), \hat{\gamma}(\tau))$. We then have the MLE triplet for the IASI and RAOB data sets as follows:

$$(\hat{\gamma}, \hat{\Delta}, \hat{\tau}),$$

which is given by Equations (5), (8), and (9).

5.3 | IASI–RAOB likelihood

The IASI observation equation is obtained by substituting Equations (3), (15), and (4) in Equation (2). This gives

$$x_{I,k}(p_j) = Z_{I,k}(p_j, \theta_j) \gamma_k - \tilde{\Delta}(p_j, \theta_j) + \varepsilon_{I,j}, \quad (16)$$

where $Z_{I,k}(p, \theta) = \int_{p_R} w(q; \theta, p) B_{R,k}(q)' dq$ and $\tilde{\Delta}(p, \theta) = \int_p^{\tilde{p}} w(q; \theta, p) \Delta(q) dq$.

Hence, the stacked IASI observation equation for the j th pressure level and all co-locations may be written as

$$X_{I,j} = Z_{I,j}(\theta_j) \gamma - \tilde{\Delta}(\theta_j) + \varepsilon_{I,j},$$

and the full data set is represented by $X_I = Z_I(\Theta) \gamma - \tilde{\Delta}(\Theta) + \varepsilon_I$, where $\Theta = (\theta_1, \dots, \theta_M)$.

Now, in order to estimate Θ , one could consider independent estimates for θ_j separately. However, this assumption contrasts with atmospheric considerations and tends to overfit. On the opposite side, one could assume $\theta(p)$ is a smooth function of p and use Bspline. This would largely increase the number of parameters to be simultaneously optimized, resulting in an unfeasible algorithm. An intermediate and suitable solution is to assume that θ is a vector random walk, namely,

$$\theta_j = \theta_{j-1} + \zeta_j, \quad (17)$$

for $j = 2, \dots, M$. In the equation above, θ_1 is an unknown parameter and the innovations ζ_j are Gaussian distributed $N(0, \Sigma_\zeta)$ with Σ_ζ a diagonal matrix.

It follows that the profile likelihood for $\gamma = \hat{\gamma}$, $\Delta = \hat{\Delta}$ and known Σ_ζ and Σ_I is given by

$$-2 \log[\zeta, X_I | \gamma, X_R, X_G] = \|Z_{I,1}(\theta_1) \gamma - \tilde{\Delta}(\theta_1)\|_{\Sigma_I} + \sum_{j=2}^M \left(\|\theta_j - \theta_{j-1}\|_{\Sigma_\zeta} + \|Z_{I,j}(\theta_j) \gamma - \tilde{\Delta}(\theta_j)\|_{\Sigma_I} \right), \quad (18)$$

which is optimized by the M nonlinear optimizations

$$\begin{aligned} \hat{\theta}_1 &= \arg \min_{\theta} \|Z_{I,1}(\theta) \gamma - \tilde{\Delta}(\theta)\|_{\Sigma_I} \\ \hat{\theta}_j &= \hat{\theta}_{j-1} + \arg \min_{\zeta} \left(\|\zeta\|_{\Sigma_\zeta} + \|Z_{I,j}(\hat{\theta}_{j-1} + \zeta) \gamma - \tilde{\Delta}(\hat{\theta}_j)\|_{\Sigma_I} \right) \end{aligned} \quad (19)$$

for $j = 2, \dots, M$, which correspond to minimizations in Equation (12). Note that the diagonal matrix Σ_I is given by the uncertainties in Equation (12), which are assumed to be known up to an acceptable approximation.

6 | CASE STUDY

In this section, the two-step harmonization procedure presented in Section 4 is applied to the RAOB–IASI data set introduced in Section 2, independently for temperature and WVMR co-locations.

6.1 | RAOB estimation

The first step is the transformation of the sparse RAOB radiosonde profiles into continuous functions to be used in the convolution of the second step. To do this, spline type and smoothing level have been chosen according to the GRUAN closeness criterion of Equation (9). Considering linear Bsplines, smoothing optimization is shown in Figures 2 and 3, giving $\hat{\tau} = 0.4$ K and $\hat{\tau} = 0.075$ g/kg for temperature and humidity, respectively. Table 1 shows that linear Bsplines with

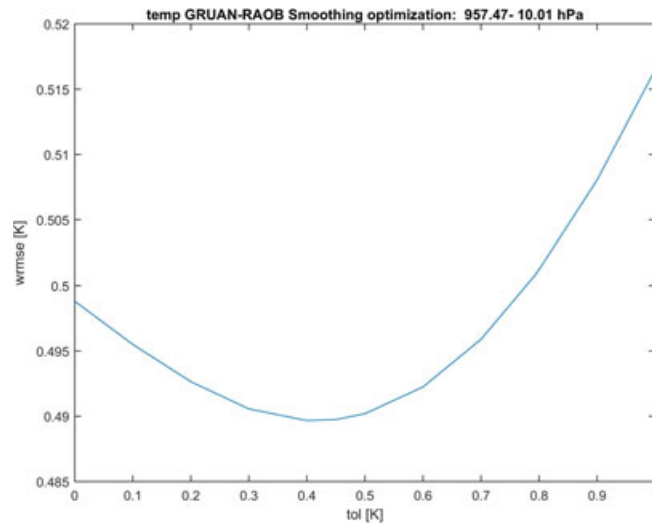


FIGURE 2 Temperature. Smoothing optimization of RAOB linear Bsplines with respect to GRUAN data in Lindenberg. (Abscissa) tolerance τ , given by Equation (7). (Ordinate) GRUAN–RAOB weighted root mean square error (wrmse). GRUAN = Global Climate Observing System Reference Upper-Air Network; RAOB = radiosonde observation

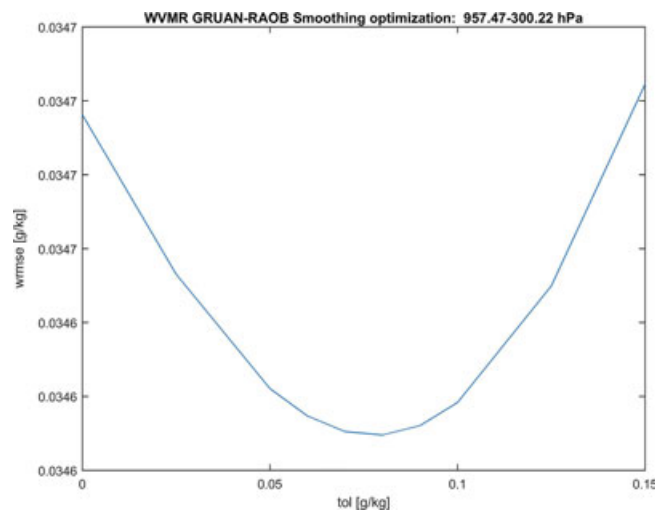


FIGURE 3 Water-vapor mixing ratio (WVMR). Smoothing optimization of radiosonde observation (RAOB) linear Bsplines with respect to Global Climate Observing System Reference Upper-Air Network (GRUAN) data in Lindenberg. (Abscissa) tolerance τ , given by Equation (7). (Ordinate) GRUAN–RAOB weighted root mean square error (wrmse)

GRUAN-optimal smoothing improve over both cubic Bsplines and interpolating Hsplines. This is consistent with the preferential sampling design characterizing RAOB significant levels mentioned in Section 4.2.

6.2 | Sparseness and processing uncertainty

The comparison of RAOB and GRUAN data in the Lindenberg station provides the GRUAN–RAOB total mismatch uncertainty, which is computed using the approach of Section 4.2. In particular, in Figures 4 and 5, $u_{RG, tot}$ of Equation (10) shows a peculiar behavior with local minima at mandatory levels. In fact, as discussed in Section 2, both RAOB and GRUAN are observed at these pressure levels, whereas between them, RAOB is observed only at significant levels. The red line interpolates between the above mentioned minima and defines the mismatch due to the difference between GRUAN data processing (Dirksen et al., 2014) and Vaisala RS92 data processing, denoted by $u_{RG, proc}$. As a result, the black dashed

TABLE 1 Comparison of linear and cubic Bsplines and interpolating Hermite splines (Hsplines) of temperature (K) and humidity (g/kg), based on the weighted root mean square error of GRUAN–RAOB in Lindenberg

| | Temperature | WVMR |
|------------------------|-------------|--------|
| Linear Bsplines | 0.4897 | 0.0346 |
| Cubic Bsplines | 0.7706 | 0.0712 |
| Interpolating Hsplines | 0.6085 | 0.0379 |

Note. WVMR = water-vapor mixing ratio; GRUAN = Global Climate Observing System Reference Upper-Air Network; RAOB = radiosonde observation.

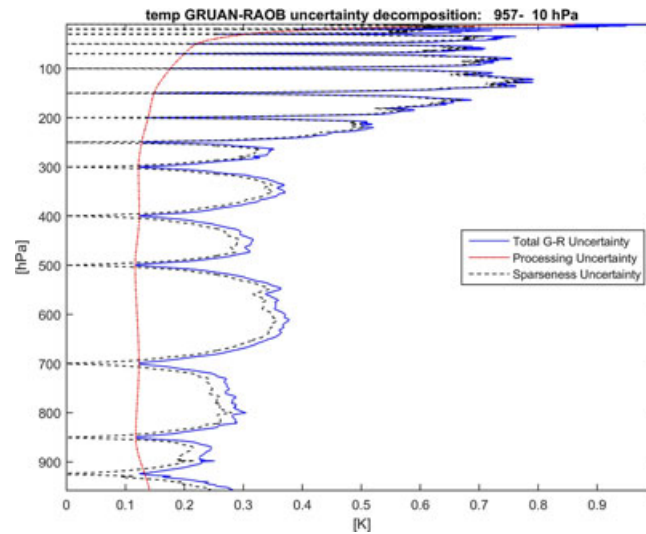


FIGURE 4 Temperature. GRUAN–RAOB mismatch uncertainties. The solid blue line is the total mismatch uncertainty ($u_{RG,tot}$), the solid red line is the uncertainty due to the difference between Vaisala and GRUAN processing ($u_{RG,proc}$), and the dashed black line is the RAOB sparseness uncertainty ($u_{R,sparse} = \sqrt{u_{RG,tot}^2 - u_{RG,proc}^2}$). GRUAN = Global Climate Observing System Reference Upper-Air Network; RAOB = radiosonde observation

line of Figures 4 and 5 is the sparseness uncertainty adjusted for mismatch in processing and is given by the quadratic difference among the previous uncertainties, namely,

$$u_{R,sparse}^2 = u_{RG,tot}^2 - u_{RG,proc}^2.$$

Considering temperature, the processing uncertainty is close to 0.1 K until 300 hPa. In this range, also sparseness uncertainty is generally smaller than 0.35 K. In the upper atmosphere, both uncertainties are larger consistently with solar radiation bias. Considering WVMR, as expected, the vertical pattern is reversed with a processing uncertainty decreasing from 0.1 g/kg at ground level to 0.02 g/kg at 300 hPa. In this range, the sparseness uncertainty is smaller than 0.3 g/kg.

6.3 | Harmonization and vertical smoothing

Conventional RAOB profiles are harmonized thanks to the optimization in Equation (19). This is solved for each IASI pressure level $p_j \in \mathbf{p}_I$ iteratively from the top pressure level $p_1 = 11$ hPa (300 hPa) and going down to $p_M = 957$ hPa separately for temperature and WVMR. We also tried to iterate in the opposite order, from ground to upper air, obtaining very close results. At each pressure level, the optimization is solved numerically. Because it is reasonable to assume that nearby pressure levels are characterized by a similar θ , the initial value for ζ is set to zero for all $j = 1, \dots, M$. To avoid local minima, the optimization for θ_1 is repeated 100 times with randomly perturbed initial values and $\hat{\theta}_1$ is taken as the optimum of these 100 solutions. The diagonal variance covariance matrix Σ_ζ , which acts as a smoothing factor has been obtained by a preliminary not regularized estimation run.

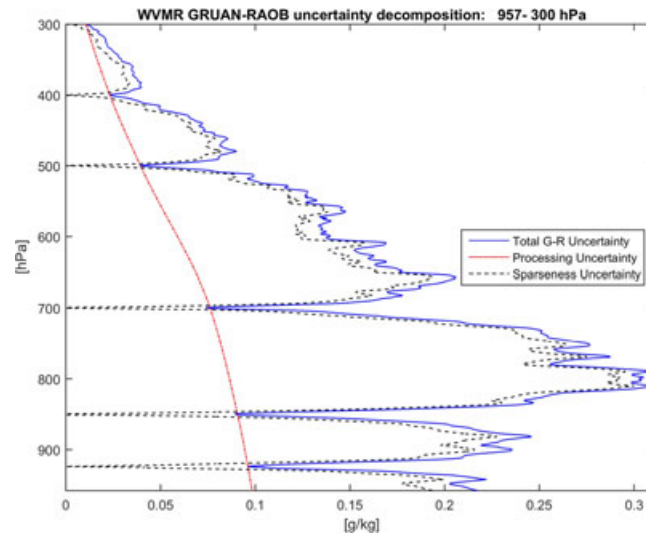


FIGURE 5 Water-vapor mixing ratio (WVMR). GRUAN–RAOB mismatch uncertainties. The solid blue line is the total mismatch uncertainty ($u_{RG.tot}$), the solid red line is the uncertainty due to the difference between Vaisala and GRUAN processing ($u_{RG.proc}$), and the dashed black line is the RAOB sparseness uncertainty ($u_{R.sparse} = \sqrt{u_{RG.tot}^2 - u_{RG.proc}^2}$). GRUAN = Global Climate Observing System Reference Upper-Air Network; RAOB = radiosonde observation

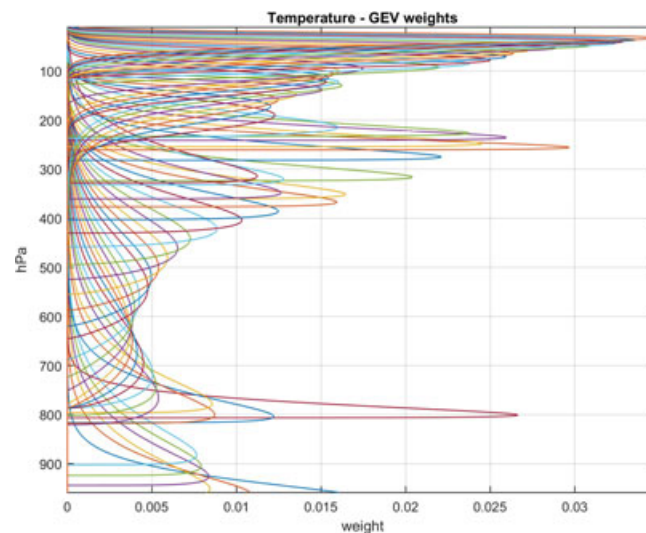


FIGURE 6 Temperature. Weight functions given by generalized extreme value (GEV) probability density functions for infrared atmospheric sounding interferometer pressure levels

In order to illustrate the results, Figures 6 and 7 show GEV pdfs $w(\cdot, \theta_j, p_j)$ related to IASI pressure levels p_1, \dots, p_M for temperature and WVMR. Each function essentially mimics how IASI sounds the atmosphere at each specific pressure level with a peak near the corresponding IASI level. The smaller the function width at pressure level p_j , the better the IASI retrieval describes the ECV at that level.

Note that, in Figure 6, the weighting functions show two peaks present near the atmospheric boundary layer (ABL; about 800 hPa) and the tropopause (about 300 hPa). In particular, the asymmetric shape of the weighting functions around the ABL clearly shows the smoothing properties of the IASI product, which is consistent with the atmosphere dynamics around the ABL. Moreover, note that the weighting function dispersion decreases at upper altitudes, implying an apparent decrease of smoothing, especially above 50 hPa. This is mainly due to the nonlinearity of the pressure scale. For instance, a pressure difference of 10 hPa at 20 hPa corresponds to an altitude difference of around 4 km, whereas the same pressure difference at 1,000 hPa corresponds to an altitude difference of only 0.08 km. Moreover, in Figure 7 weight functions near 300 hPa are clearly affected by a border effect and should be interpreted with caution.

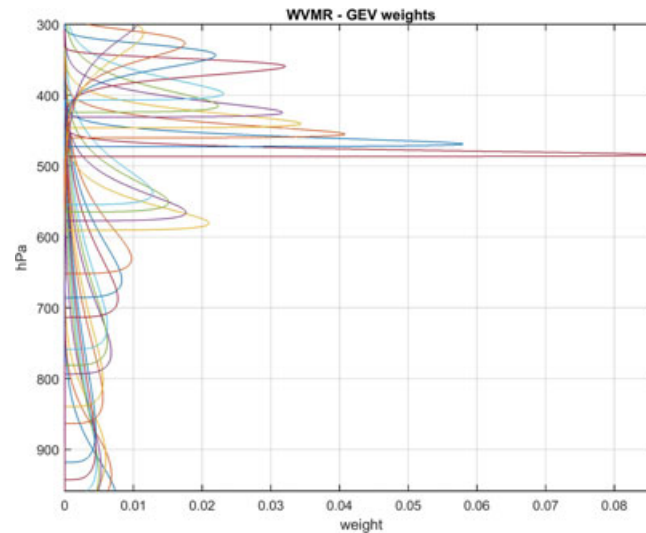


FIGURE 7 Generalized extreme values (WVMR). Weight functions given by generalized extreme value (GEV) probability density functions for infrared atmospheric sounding interferometer pressure levels

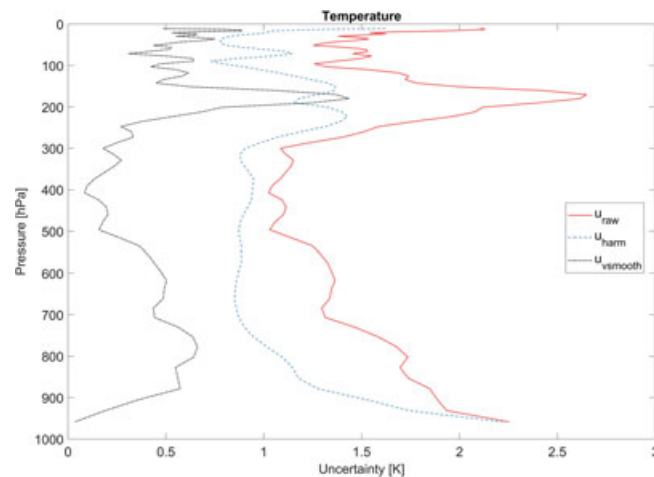


FIGURE 8 Temperature. (Black dotted line) vertical smoothing uncertainty, $u_{\text{RI.vsmooth}}$, is the uncertainty due to the difference in smoothing between radiosonde observation (RAOB) and infrared atmospheric sounding interferometer (IASI). The profile average is 0.501 K. (Cyan dashed line) harmonized mismatch uncertainty, $u_{\text{RI.harm}}$, is the uncertainty due to the mismatch after adjusting for difference in vertical smoothing. The profile average is 1.052 K. (Red solid line) unadjusted uncertainty, $u_{\text{RI.raw}}$, is the total uncertainty between interpolated RAOB and IASI. The profile average is 1.553 K. The formulas are given in Section 4.4

After harmonizing RAOB to IASI, the adjusted uncertainty of Equation (14) is computed and the related vertical smoothing uncertainty decomposition of Equation (13) is reported in Figures 8 and 9. The IASI–RAOB comparison is dominated by the smoothness of the IASI retrieval and its reduced capability to catch strong vertical gradients with respect to the RAOB profiles, though their sparseness. In the boundary layer (BL) below about 900 hPa, where significant inversion in the temperature profiles may occur, the harmonization does not strongly reduce the raw uncertainty, but above, up to 700 hPa, the reduction becomes more significant. In the upper troposphere/lower stratosphere, the strong gradients at the tropopause increase the raw uncertainty and the harmonization strongly reduces the difference between IASI and RAOB. It is worth to remind that the values calculated above 100 hPa are affected by the size of the sampling, which is more limited than at higher pressure levels. For WVMR, results similar to temperature are observed in the BL. The increase of the smoothness uncertainty at 800 hPa is likely linked to the transition from wetter to drier air occurring at the top of BL not always caught in the RAOB data. The benefit of the harmonization decreases with the altitude proportionally with the decrease of the water vapor variability in the atmosphere. This is clearly visible from the difference between the raw and harmonized uncertainties, which reduces with the height.

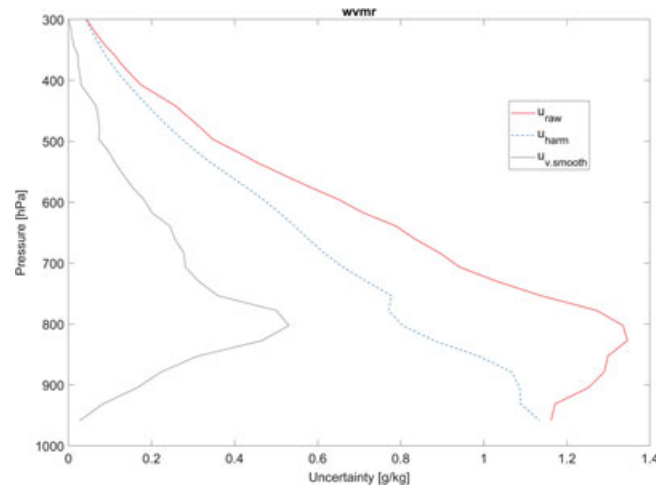


FIGURE 9 Water-vapor mixing ratio (WVMR). (Black dotted line) vertical smoothing uncertainty, $u_{\text{RI.vsmooth}}$, is the uncertainty due to the difference in smoothing between radiosonde observation (RAOB) and infrared atmospheric sounding interferometer (IASI). The profile average is 0.1632 g/kg. (Cyan dashed line) harmonized mismatch uncertainty, $u_{\text{RI.harm}}$, is the uncertainty due to the mismatch after adjusting for the difference in vertical smoothing. The profile average is 0.4833 g/kg. (Red solid line) unadjusted uncertainty, u_{raw} , is the raw uncertainty between the interpolated RAOB and IASI. The profile average is 0.6465 g/kg. The formulas are given in Section 4.4

7 | DISCUSSION AND CONCLUSION

This paper discussed the comparison of IASI and RAOB temperature and humidity with a focus on vertical smoothing. Because the IASI averaging kernels have been considered unknown, a weighting function mimicking the weights of the averaging kernel has been estimated on data. The behavior of the estimated weighting functions has been found to be consistent with atmospheric dynamics around both the tropopause and the ABL. In order to do this, RAOB data have been transformed into functional data and the related uncertainty has been assessed by a comparison with the reference measurements for radiosonde given by GRUAN data, Lindenberg. Hence, it can be considered as a first substantial step in the direction of Calbet et al. (2017), “to fully characterize the comparison, a method to estimate the collocation uncertainty would be desirable. This method should not depend on the data being used for the study and should be independent from them.”

Thanks to this approach, it has been found that the uncertainty of vertical smoothing mismatch averaged along the profile is 0.50 K for temperature and 0.16 g/kg for WVMR. Although some uncertainty components have not been taken into account, the vertical smoothing uncertainty is correct under incorrelation assumption. Moreover, the uncertainty related to RAOB vertical sparseness, averaged along the profile, is 0.29 K for temperature and 0.13 g/kg for WVMR. Notice that, because RAOB data are obtained mainly but not exclusively by Vaisala RS92 sondes, vertical sparseness uncertainty assessment is valid for the Central European area but should be used with some cautions for SRS and MODEM sondes. On the other side, the vertical smoothing uncertainty embeds the RAOB heterogeneity and, hence, is valid for the entire area.

From the methodological point of view, it has been shown that the estimates are obtained by the maximum likelihood method, taking into consideration also the measurement uncertainties where available.

7.1 | Further developments

Further aspects may be added to the present analysis of satellite versus radiosonde comparison. For instance, the distance between the satellite line of sight and the radiosonde position has not been considered. In fact, this issue will be addressed in a forthcoming paper using isotonic regression (Meyer, 2013).

Vertical correlation has not been considered explicitly here and, in this sense, the results could be suboptimal. In fact, IASI measurements are known to have a limited number of degrees of freedom. In our approach, at least a part of IASI vertical correlation is implicitly handled by the random walk dynamics of GEV pdf parameters in Section 5.3. Considering radiosonde, sources of vertical correlation arise both from short-range smoothing algorithms, used to avoid measurement outliers, and by prelaunch calibration errors. Although a good part of these problems is automatically handled by the functional data approach used here, further research could point out new solutions.

A further insight into vertical smoothing could benefit from the comparison of this proposal with the IASI “true averaging kernel” at least in some cases. Nonetheless, we remark that the approach of this paper can be used even in absence of averaging kernels, which is quite relevant especially for historical records.

ACKNOWLEDGEMENTS

This research is partially funded by GAIA-CLIM, the project funded from the European Commission's Horizon 2020 research and innovation programme under grant agreement 640276. We are very thankful to NOAA and in particular to Tony Reale for providing the radiosonde-satellite collocations. We also thank the anonymous reviewers for their insightful comments.

ORCID

F. Finazzi  <http://orcid.org/0000-0002-1295-7657>

REFERENCES

- Berrisford, P., Dee, D. P., Fielding, K., Fuentes, M., Kållberg, P., Kobayashi, S., & Uppala, S. M. (2009). *The ERA-interim archive* (ERA Report Series, No. 1). Reading, UK: European Centre for Medium-Range Weather Forecasts.
- Bojinski, S., Verstraete, M., Peterson, T. C., Richter, C., Simmons, A., & Zemp, M. (2014). The concept of essential climate variables in support of climate research, applications, and policy. *Bulletin of the American Meteorological Society*, 95, 1431–1443. <https://doi.org/10.1175/bams-d-13-00047.1>
- Calbet, X., Peinado-Galan, N., Ripodas, P., Trent, T., Dirksen, R., & Sommer, M. (2017). Geostatistical inference under preferential sampling. *Atmospheric Measurement Techniques*, 10(6), 2323–2335. <https://doi.org/10.5194/amt-10-2323-2017>
- Diggle, P. J., Menezes, R., & Su, T. (2010). Geostatistical inference under preferential sampling. *Journal of the Royal Statistical Society: Series C (Applied Statistics)*, 59, 191–232. <https://doi.org/10.1111/j.1467-9876.2009.00701.x>
- Dirksen, R. J., Sommer, M., Immler, F. J., Hurst, D. F., Kivi, R., & Vömel, H. (2014). Reference quality upper-air measurements: GRUAN data processing for the Vaisala RS92 radiosonde. *Atmospheric Measurement Techniques*, 7, 4463–4490. <https://doi.org/10.5194/amt-7-4463-2014>
- Fahrmeir, L., Kneib, T., Lang, S., & Marx, B. (2013). *Regression—Models, methods and applications*. Berlin, Germany: Springer.
- Fassò, A., Ignaccolo, R., Madonna, F., Demoz, B., & Franco-Villoria, M. (2014). Statistical modelling of collocation uncertainty in atmospheric thermodynamic profiles, 7, 1803–1816.
- Fassò, A., Verhoelst, T., & Lambert, J. C. (2018). Report of the Gap Analysis for Integrated Atmospheric ECV CLimate Monitoring. *Report on the scientific assessment of gaps using a statistical approach, GAIA-CLIM deliverable D1.10*. <http://www.gaia-clim.eu/page/deliverables>
- Ignaccolo, R., Franco-Villoria, M., & Fassò, A. (2015). Modelling collocation uncertainty of 3D atmospheric profiles. *Stochastic Environmental Research and Risk Assessment*, 29(2), 417–429.
- Immler, F. J., Dykema, J., Gardiner, T., Whiteman, D. N., Thorne, P. W., & Vömel, H. (2010). Reference quality upper-air measurements: Guidance for developing GRUAN data products. *Atmospheric Measurement Techniques*, 3, 1217–1231. <https://doi.org/10.5194/amt-3-1217-2010>
- Kotz, S., & Nadarajah, S. (2000). *Extreme value distributions: Theory and applications*. London, UK: Imperial College Press.
- Kursinski, E. R., & Hajj, G. A. (2001). A comparison of water vapor derived from GPS occultations and global weather analyses. *Journal of Geophysical Research*, 106, 1113–1138.
- Lambert, J. -C., & Vandenbussche, S. (2011). *Multi-dimensional characterisation of remotely sensed data* (EC FP6 GEOMon Technical Note D4.2.1). Chapter 1: Ground-based measurements, GEOMon TN-IASB-OBSOP/Chapter 1, BIRA-IASB. 8033, 8034, 8036.
- Maddy, E. S., & Barnet, C. D. (2008). Vertical resolution estimates in version 5 of AIRS operational retrievals. *IEEE Transactions on Geoscience and Remote Sensing*, 46, 2375–2384.
- Meyer, M. C. (2013). A simple new algorithm for quadratic programming with applications in statistics. *Communications in Statistics*, 42(5), 1126–1139.
- Pappalardo, G., Wandinger, U., Lucia, M., Hiebsch, A., Mattis, I., Amodeo, A., ... Ansmann, A. (2010). EARLINET correlative measurements for CALIPSO: First intercomparison results. *Journal of Geophysical Research*, 115, D00H19. <https://doi.org/10.1029/2009JD012147>
- Pougatchev, N., August, T., Calbet, X., Hultberg, T., Oduleye, O., Schlüssel, P., ... Bingham, G. (2009). IASI temperature and water vapor retrievals – error assessment and validation. *Atmospheric Chemistry and Physics*, 9, 6453–6458. <https://doi.org/10.5194/acp-9-6453-2009>
- Ramsay, J., & Silverman, B. (2012). *Applied functional data analysis: Methods and case studies*. New York, NY: Springer.
- Reinsch, C. (1971). Smoothing by spline functions II. *Numerische Mathematik*, 16, 451–454.
- Ridolfi, M., Blum, U., Carli, B., Catoire, V., Ceccherini, S., Claude, S., ... Wetzell, H. (2007). Geophysical validation of temperature retrieved by the ESA processor from MIPAS/ENVISAT atmospheric limb-emission measurements. *Atmospheric Chemistry and Physics*, 7, 4459–4487. <https://doi.org/10.5194/acp-7-4459-2007>
- Seidel, D. J., Sun, B., Petty, M., & Reale, A. (2011). Global radiosonde balloon drift statistics. *Journal of Geophysical Research*, 116, D07102. <https://doi.org/10.1029/2010JD014891>

- Sun, B., Reale, A., Tilley, F., Petty, M., Nalli, N. R., & Barnett, C. D. (2017). Assessment of NUCAPS S-NPP CrIS/ATMS sounding products using reference and conventional radiosonde observations. *IEEE Journal of Selected Topics in Applied Earth Observations and Remote Sensing*, 10(6), 2499–2509. <https://doi.org/10.1109/JSTARS.2017.2670504>
- Tobin, D. C., Revercomb, H. E., Knuteson, R. O., Lesht, B. M., Strow, L. L., Hannon, S. E., ... Cress, T. S. (2006). Atmospheric Radiation Measurement site atmospheric state best estimates for Atmospheric Infrared Sounder temperature and water vapor retrieval validation. *Journal of Geophysical Research*, 111, D09S14. <https://doi.org/10.1029/2005JD006103>
- Verhoelst, T., Granville, J., Hendrick, F., Köhler, U., Lerot, C., Pommereau, J.-P., ... Lambert, J.-C. (2015). Metrology of ground-based satellite validation: Co-location mismatch and smoothing issues of total ozone comparisons. *Atmospheric Measurement Techniques*, 8, 5039–5062. <https://doi.org/10.5194/amt-8-5039-2015>

How to cite this article: Finazzi F, Fassò A, Madonna F, Negri I, Sun B, Rosoldi M. Statistical harmonization and uncertainty assessment in the comparison of satellite and radiosonde climate variables. *Environmetrics*. 2018;e2528. <https://doi.org/10.1002/env.2528>